

Sensitive magnetic-field-response magnetization dynamics in a one-dimensional dysprosium coordination polymer

Yun-Xia Qu, Ze-Yu Ruan, Guo-Zhang Huang, Yan-Cong Chen, Yang Liu, Jian-Hua Jia, Jun-Liang Liu* and Ming-Liang Tong*

Key Laboratory of Bioinorganic and Synthetic Chemistry of Ministry of Education, School of Chemistry, Sun Yat-Sen University, Guangzhou 510006, China

Contents

S1. Experimental section.....	2
S2. Crystal Data and Structures.....	3
S3. Magnetic Characterization.....	8
S4. Photoluminescence Spectra.....	14
S5. <i>Ab initio</i> Calculations.....	16
S6. References.....	18

1. Experimental section

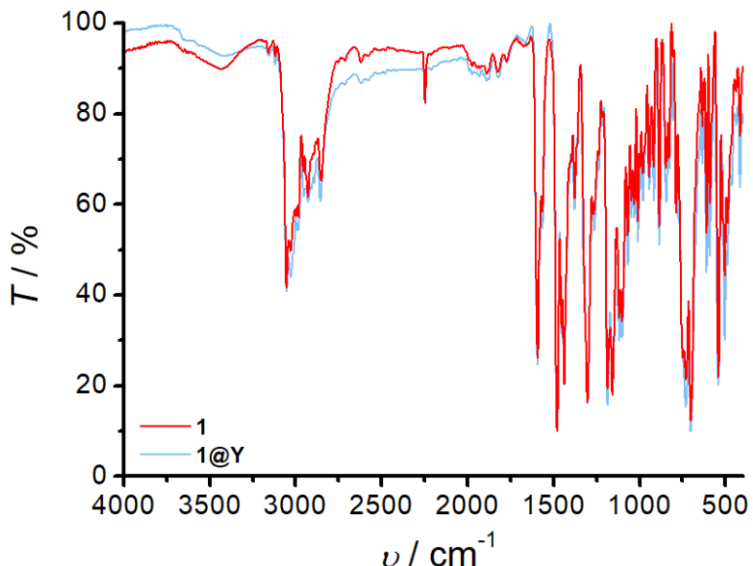


Figure S1. Infrared spectra for **1** and **1@Y**.

Computational Details.

All *ab initio* calculations were carried out with OpenMOLCAS version 18.09¹ and are of the CASSCF/RASSI type. The Cholesky decomposition threshold was set to 1×10^{-8} to save disk space. A fragment of polymer, in which the hexylene groups being replaced with propyl groups, was included, and the coordinates of atoms were extracted from the experimentally determined crystal structure. ANO-RCC-VTZP basis set approximations have been employed for Dy, P, O and N atoms, ANO-RCC-VTZ for C and H atoms.²⁻⁴ Active space of the CASSCF method included nine electrons in seven 4f orbitals of Dy(III). 21 sextets were optimized in state-averaged calculations, and then 21 sextets were mixed by spin-orbit coupling using RASSI approach.⁵ The g-tensors, energies, main magnetic axis as well as the magnetizations were obtained by SINGLE_ANISO routine.⁶

Magnetic Measurements

Magnetic susceptibility measurements were collected using a Quantum Design MPMS-XL7 SQUID magnetometer and a Quantum Design PPMS, and a Quantum Design MPMS3. Polycrystalline samples were embedded in vaseline to prevent torqueing. All data were corrected for the diamagnetic contribution.

2. Crystal Data and Structures

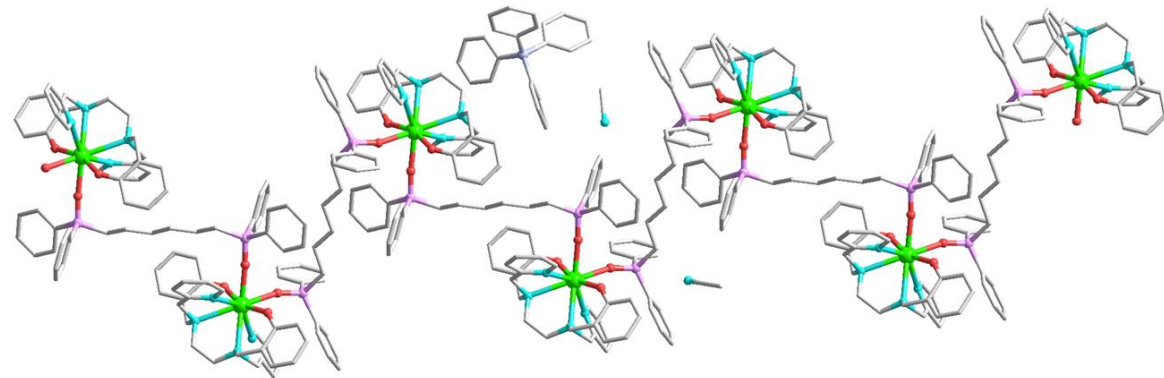


Figure S2. 1D crystal structure of **1**. Color Codes: Dy , green; N , blue; P , purplish red; B , purple; O , red; C , gray. Hydrogen atoms are omitted for clarity.

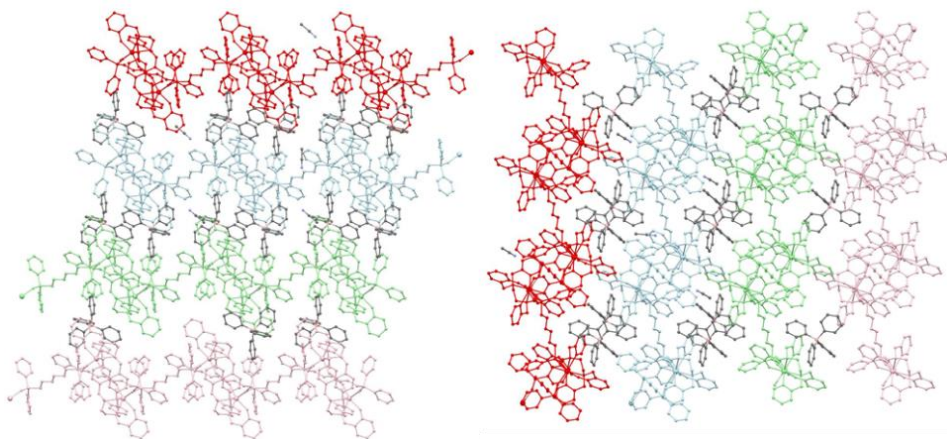


Figure S3. Crystal structure of **1** viewed along the b and c axis. H atoms are omitted for clarity.

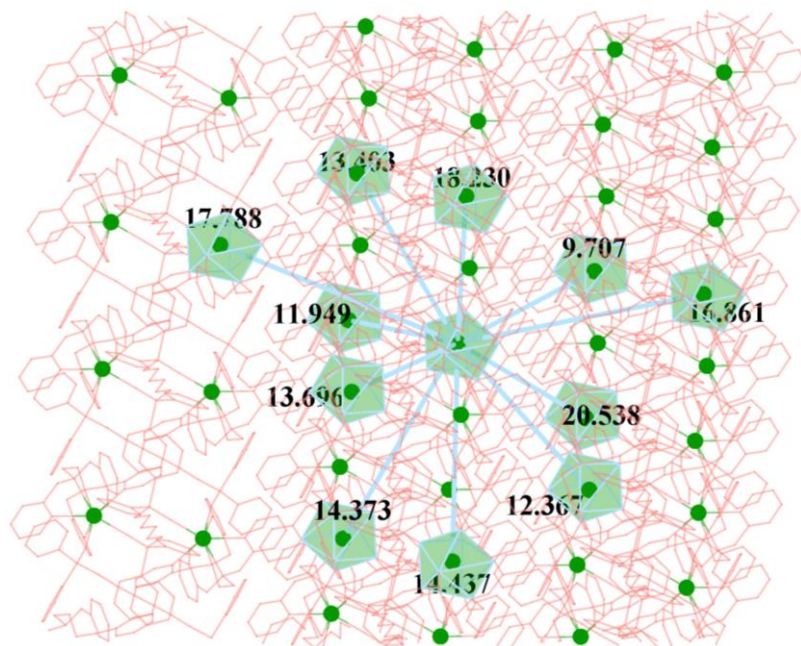


Figure S4. Intermolecular Dy-Dy distances, where the shortest one is 9.707 Å.

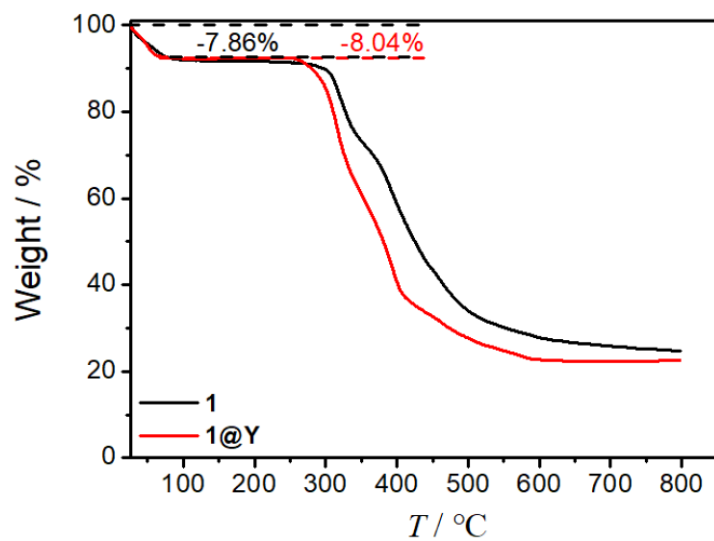


Figure S5. Thermogravimetric analysis for **1** and **1@Y** under N₂ atmosphere (10 K min⁻¹). The dashed lines correspond to the theoretical weight loss percentage of 2 MeCN and 2 H₂O.

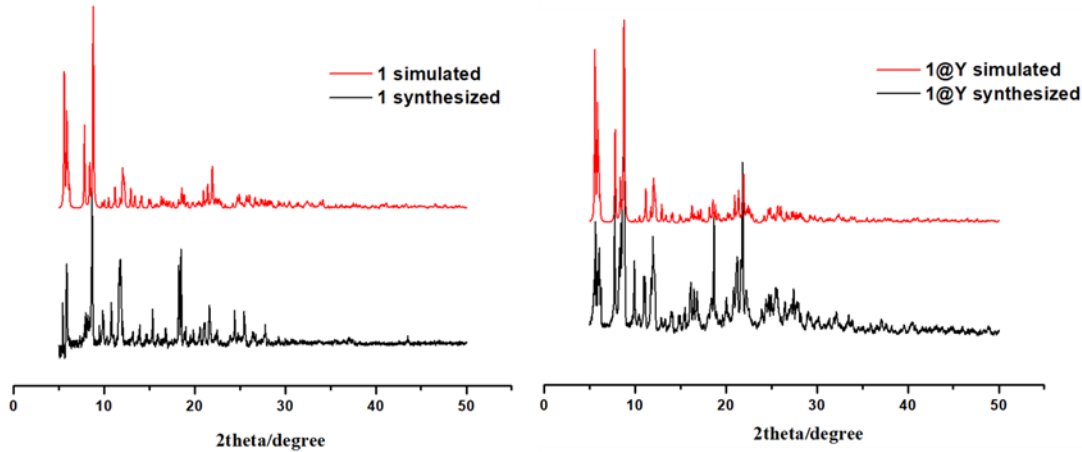


Figure S6. PXRD patterns of **1** (left) and **1@Y** (right) compared with the simulated pattern from the single-crystal structures.

Table S1. Continuous Shape Measures calculations (CShM) for **1** and **1@Y**.⁷

Complex	OP (D _{8h})	HPY-8 (C _{7v})	HBPY-8 (D _{6h})	CU-8 (O _h)	SAPR-8 (D _{4d})	TDD-8 (D _{3d})	JGBF-8 (D _{3d})					
1	32.61912	21.14305	11.98907	8.17713	1.61131	2.56987	11.95869					
1@Y	32.63058	21.15545	12.05724	8.18014	1.57190	2.56161	12.05322					
Complex	JETBPY-8 (D _{3h})		JBTPR-8 (C _{2v})		BTPR-8 (C _{2v})		JSD-8 (D _{2d})		TT-8 (T _d)		ETBPY-8 (D _{3h})	
1	27.56682		2.90835		2.63793		4.85210		8.98807		23.04509	
1@Y	27.68220		2.89480		2.61828		4.84097		8.98859		23.16292	

OP-8 = Octagon, HPY-8 = Heptagonal pyramid, HBPY-8 = Hexagonal bipyramid, CU-8 = Cube, SAPR-8 = Square antiprism, TDD-8 = Triangular dodecahedron, JGBF-8 = Johnson gyrobifastigium J26, JETBPY-8 = Johnson elongated triangular bipyramid J14, JBTPR-8 = Biaugmented trigonal prism J50, BTPR-8 = Biaugmented trigonal prism, JSD-8 = Snub diphenoid J84, TT-8 = Triakis tetrahedron, ETBPY-8 = Elongated trigonal bipyramid

Table S2. Crystal data and structure refinement parameters for **1** and **1@Y**

	1	1@Y
Empirical formula	C ₈₆ H ₉₀ BDyN ₆ O ₆ P ₂	C ₈₆ H ₉₀ BN ₆ O ₆ P ₂ Y _{0.95} Dy _{0.05}
Formula weight	1538.88	1469.02
Temperature/K	120(2)	150(2)
Crystal system	triclinic	triclinic
Space group	<i>P</i> -1	<i>P</i> -1
<i>a</i> /Å	14.4368(9)	14.4603(10)
<i>b</i> /Å	16.8612(11)	16.8841(13)
<i>c</i> /Å	17.7877(13)	17.8153(13)

$\alpha/^\circ$	116.577(2)	116.529(2)
$\beta/^\circ$	95.674(2)	95.822(2)
$\gamma/^\circ$	90.602(2)	90.434(2)
Volume/ \AA^3	3846.1(5)	3864.7(5)
Z	2	2
$\rho_{\text{calc}}/\text{g cm}^{-3}$	1.329	1.231
μ/mm^{-1}	1.070	0.860
$F(000)$	1594	1503
Radiation/ \AA	Mo- $K\alpha$ ($\lambda = 0.71073$)	Mo- $K\alpha$ ($\lambda = 0.71073$)
Reflections collected	14686	43447
Independent reflections	17620 [$R_{\text{int}} = 0.0754$, $R_{\text{sigma}} = 0.0565$]	14290 [$R_{\text{int}} = 0.0839$, $R_{\text{sigma}} = 0.0918$]
Goodness-of-fit on F^2	1.037	1.005
Final R indexes [$I >= 2\sigma(I)$]	$R_1 = 0.0324$, $wR_2 = 0.0649$	$R_1 = 0.0490$, $wR_2 = 0.0985$
Final R indexes [all data]	$R_1 = 0.0478$, $wR_2 = 0.0691$	$R_1 = 0.0985$, $wR_2 = 0.1156$
Largest diff. peak/hole/e \AA^{-3}	0.62/-0.80	0.39/-0.75
CCDC no.	1975686	2031584

^a $R_1 = \sum|F_o| - |F_c|/|\sum|F_o||$;

^b $wR_2 = \{[\sum w(F_o^2 - F_c^2)^2]/[\sum w(F_o^2)^2]\}^{1/2}$.

Table S3. Selected bond lengths [\AA] and angles [$^\circ$] for **1** and **1@Y**

Bond lengths	1	1@Y	Bond angles	1	1@Y
Dy-N1	2.5841(19)	2.577(3)	N1-Dy-N2	62.46(6)	62.40(8)
Dy-N2	2.674(2)	2.672(3)	N1-Dy-N3	83.16(6)	82.96(8)
Dy-N3	2.6725(19)	2.669(3)	N3-Dy-N2	68.04(6)	67.88(8)
Dy-N4	2.5784(19)	2.565(3)	N4-Dy-N1	140.45(6)	140.09(8)
Dy-O1	2.2116(17)	2.213(2)	N4-Dy-N2	86.57(6)	86.15(8)
Dy-O2	2.2244(17)	2.221(2)	N4-Dy-N3	61.64(6)	61.63(8)
Dy-O3	2.3567(16)	2.343(2)	O1-Dy-N1	80.33(6)	80.52(8)
Dy-O4	2.3127(15)	2.298(2)	O1-Dy-N2	126.58(6)	126.52(8)
			O1-Dy-N3	70.85(6)	70.68(8)
			O1-Dy-N4	102.48(6)	102.49(8)
			O1-Dy-O2	159.92(6)	160.10(8)
			O1-Dy-O3	81.99(6)	81.81(7)
			O1-Dy-O4	83.94(6)	84.20(7)
			O2-Dy-N1	107.91(6)	107.83(8)
			O2-Dy-N2	72.60(6)	72.55(8)
			O2-Dy-N3	127.46(6)	127.41(8)

O2-Dy-N4	82.99(6)	82.86(8)
O2-Dy-O3	81.43(6)	81.72(7)
O2-Dy-O4	81.83(6)	81.86(7)
O3-Dy-N1	145.98(6)	146.30(7)
O3-Dy-N2	148.13(6)	148.11(7)
O3-Dy-N3	117.73(6)	117.49(8)
O3-Dy-N4	71.95(6)	71.98(8)
O4-Dy-N1	70.51(6)	70.49(8)
O4-Dy-N2	114.33(6)	114.29(8)
O4-Dy-N3	146.28(6)	146.15(8)
O4-Dy-N4	148.80(6)	149.13(8)
O4-Dy-O3	78.92(5)	79.37(7)

3. Magnetic Characterization

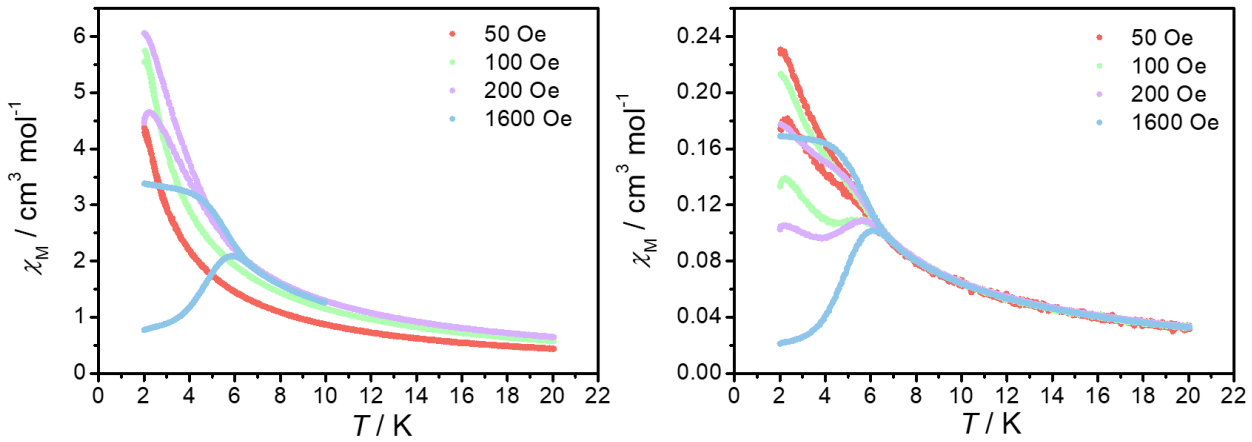


Figure S7. Zero-field-cooled/field-cooled (ZFC-FC) magnetic susceptibilities (warm mode, 2 K min^{-1}) for **1** (left) and **1@Y** (right).

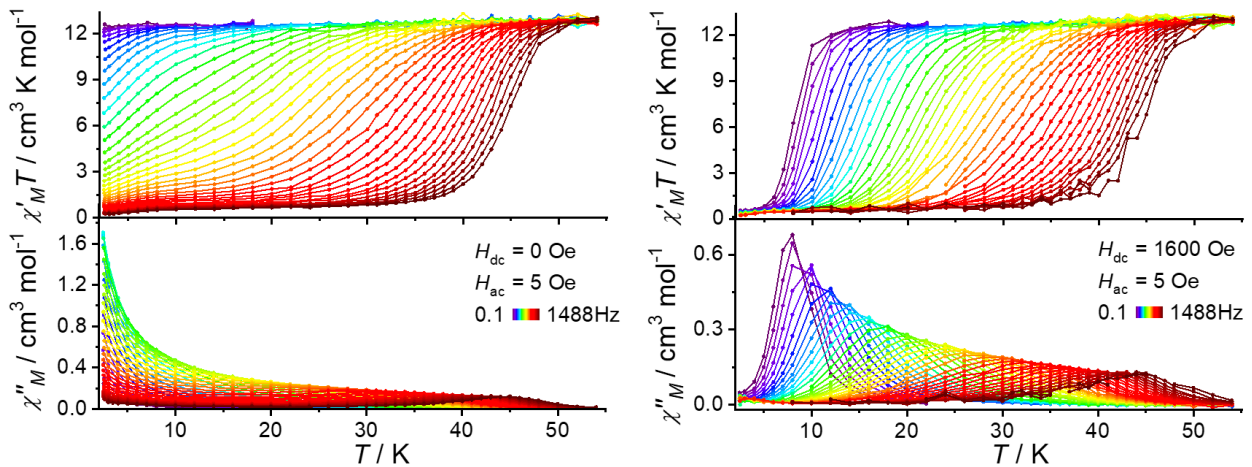


Figure S8. Temperature dependence of the in-phase ($\chi'_M T$) and out-of-phase (χ''_M) components of the ac magnetic susceptibility for **1** under 0 (left) and 1600 Oe (right) applied dc field with the ac frequency of 0.1-1488 Hz.

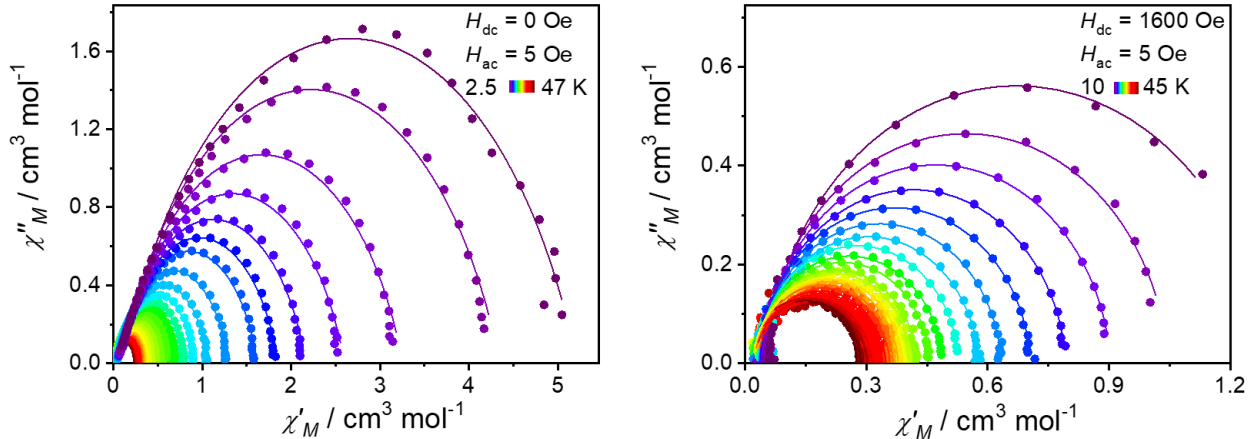


Figure S9. Cole-Cole plots for the determination of the temperature dependence of τ for pure **1** under zero (left) and 1600 Oe (right) dc applied field. Solid lines are the results of best fits to the generalized Debye model as described in the main text.

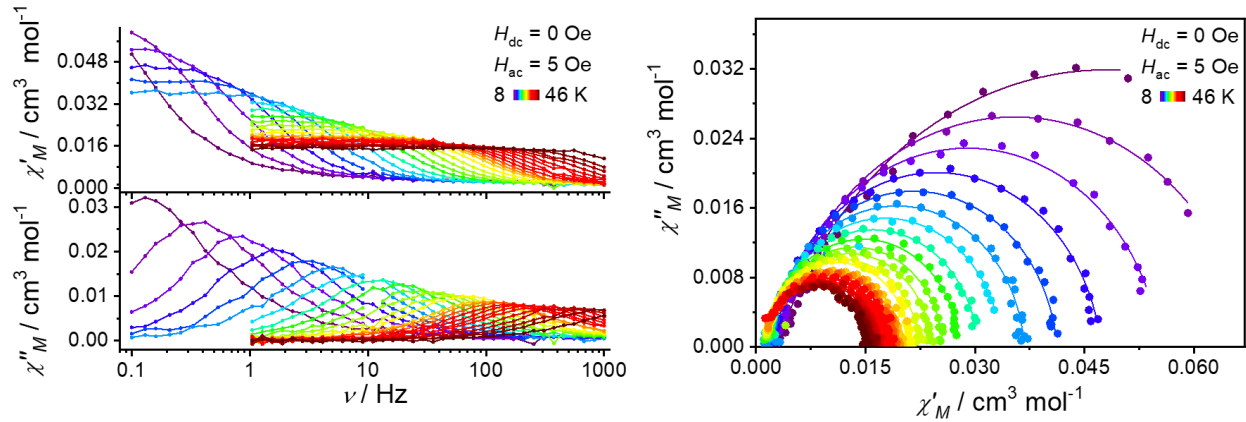


Figure S10. Frequency-dependence of the in-phase ($\chi_M'T$) product and out-of-phase (χ_M'') under zero dc field for **1@Y** with the ac frequency of 0.1-999 Hz. The solid lines are guides for the eyes (left). Cole-Cole plots of **1@Y** at 8-46 K under zero dc field ($\alpha = 0-0.214$), and solid lines are best fits for the generalized Debye model (right).

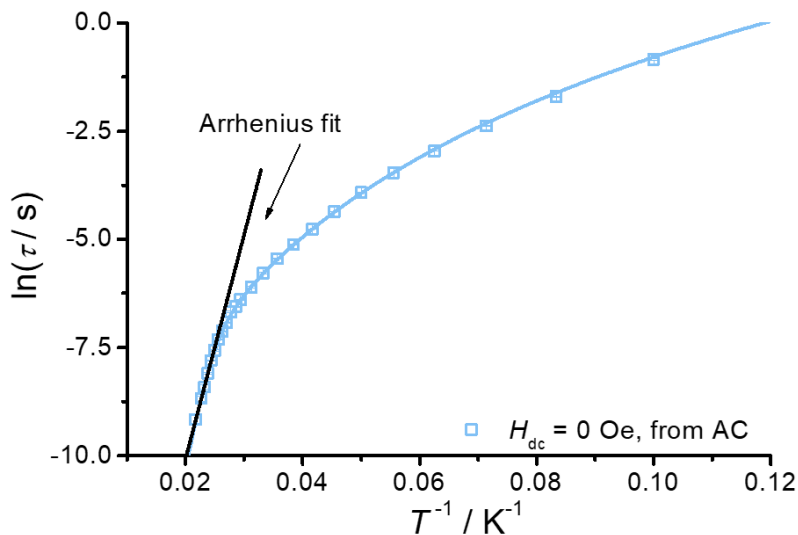


Figure S11. Temperature dependence of the relaxation time τ under zero dc field for **1@Y**. The solid lines are best fits to the Arrhenius law, and the dashed lines are best fits to the multiple relaxation equation.

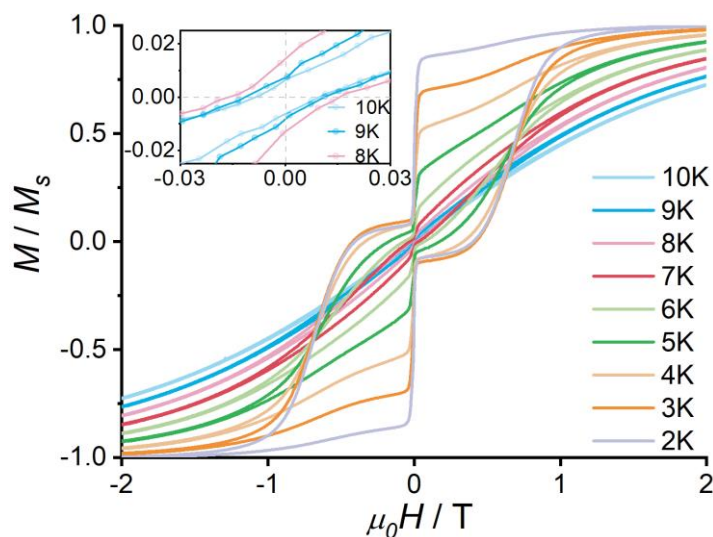


Figure S12. Normalized magnetic hysteresis loops for **1@Y**. The data were continuously collected at intervals of 1 s with the field ramping speed of 200 Oe/s at various temperatures. The expanded views (inset) reveal clear magnetic hysteresis to 9 K. For all temperatures below, the loops are open at zero field.

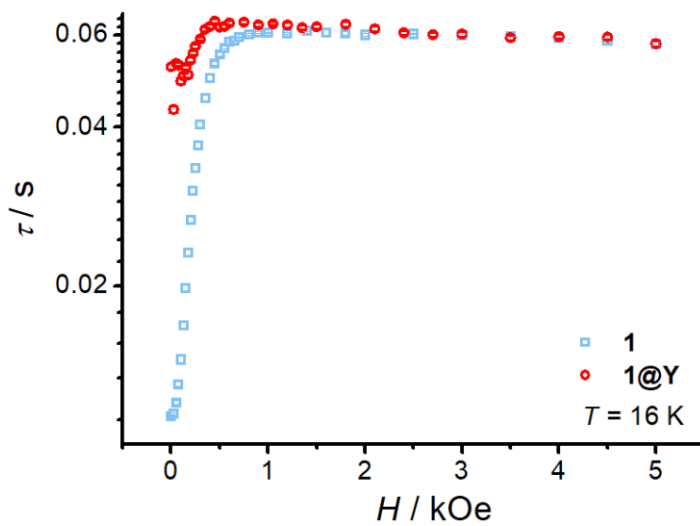


Figure S13. Field dependence of the relaxation time for **1** and **1@Y** extracted from the single-relaxation-time model.

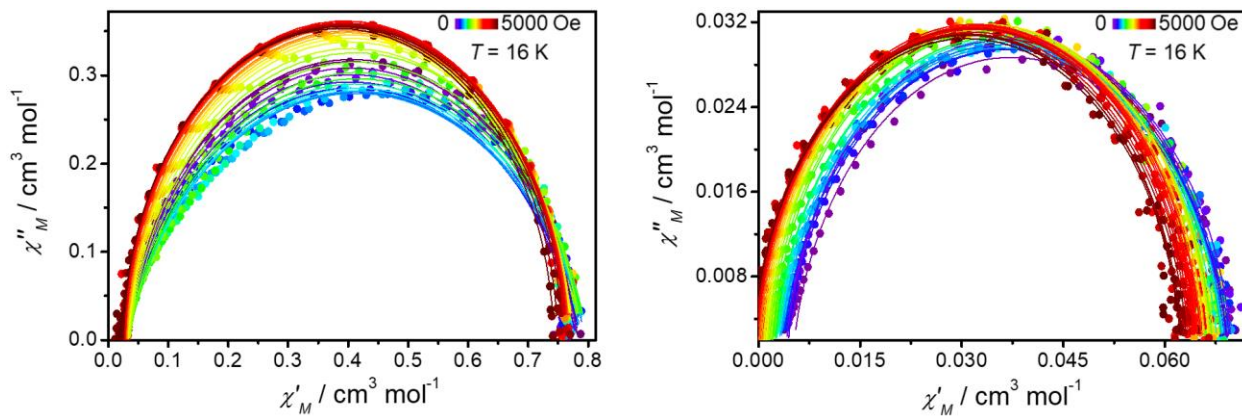


Figure S14. Cole-Cole plots of **1** (*left*) and **1@Y** (*right*) at 16 K under 0-5000 Oe dc field, and solid lines are best fits for the generalized Debye model.

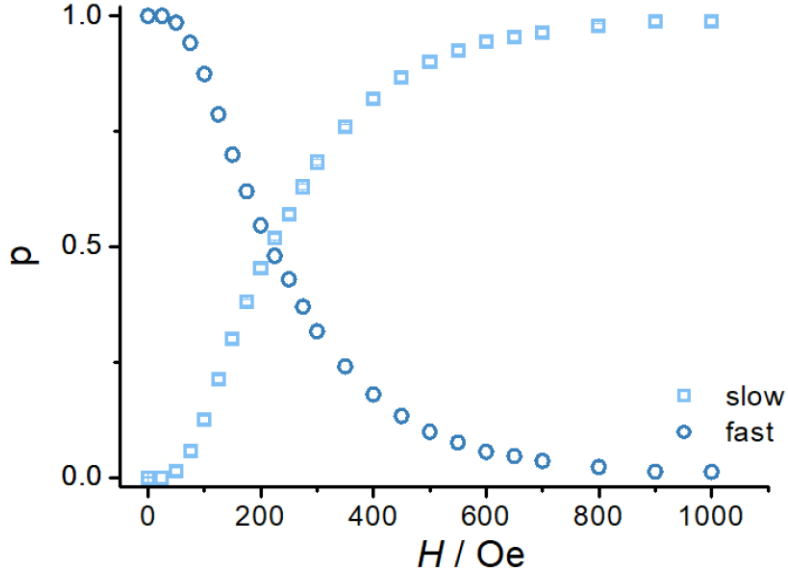


Figure S15. Field dependence of the relaxation time for **1** extracted from the double-relaxation-time model⁸. p is the proportion of two relaxation times: one is fast relaxation (deep blue); another is slow one (light), with $\tau_1 = 0.0595(2)$ s, $\tau_2 = 0.01179(7)$ s, respectively.

The formula of double-relaxation-time model is shown as follows:

$$\chi(\omega) = \chi_s + p \frac{\chi_T - \chi_s}{1 + (i\omega\tau_1)^{1-\alpha}} + (1-p) \frac{\chi_T - \chi_s}{1 + (i\omega\tau_2)^{1-\alpha}} \quad \text{Eqn(S1)}$$

$$\begin{aligned} \chi'(\omega) &= \chi_s + p (\chi_T - \chi_s) \frac{1 + (\omega\tau_1)^{1-\alpha_1} \sin(\pi\alpha_1/2)}{1 + 2(\omega\tau_1)^{1-\alpha_1} \sin(\pi\alpha_1/2) + (\omega\tau_1)^{2-2\alpha_1}} \\ &\quad + (1-p)(\chi_T - \chi_s) \frac{1 + (\omega\tau_2)^{1-\alpha_2} \sin(\pi\alpha_2/2)}{1 + 2(\omega\tau_2)^{1-\alpha_2} \sin(\pi\alpha_2/2) + (\omega\tau_2)^{2-2\alpha_2}} \end{aligned}$$

$$\begin{aligned} \chi''(\omega) &= p (\chi_T - \chi_s) \frac{(\omega\tau_1)^{1-\alpha_1} \cos(\pi\alpha_1/2)}{1 + 2(\omega\tau_1)^{1-\alpha_1} \sin(\pi\alpha_1/2) + (\omega\tau_1)^{2-2\alpha_1}} \\ &\quad + (1-p)(\chi_T - \chi_s) \frac{(\omega\tau_2)^{1-\alpha_2} \cos(\pi\alpha_2/2)}{1 + 2(\omega\tau_2)^{1-\alpha_2} \sin(\pi\alpha_2/2) + (\omega\tau_2)^{2-2\alpha_2}} \end{aligned}$$

χ_T and χ_s are the isothermal and adiabatic limit of the susceptibility, respectively. The wider the distribution in relaxation times the larger is α , and $\alpha_1 = 0.000(3)$, $\alpha_2 = 0.125(2)$.

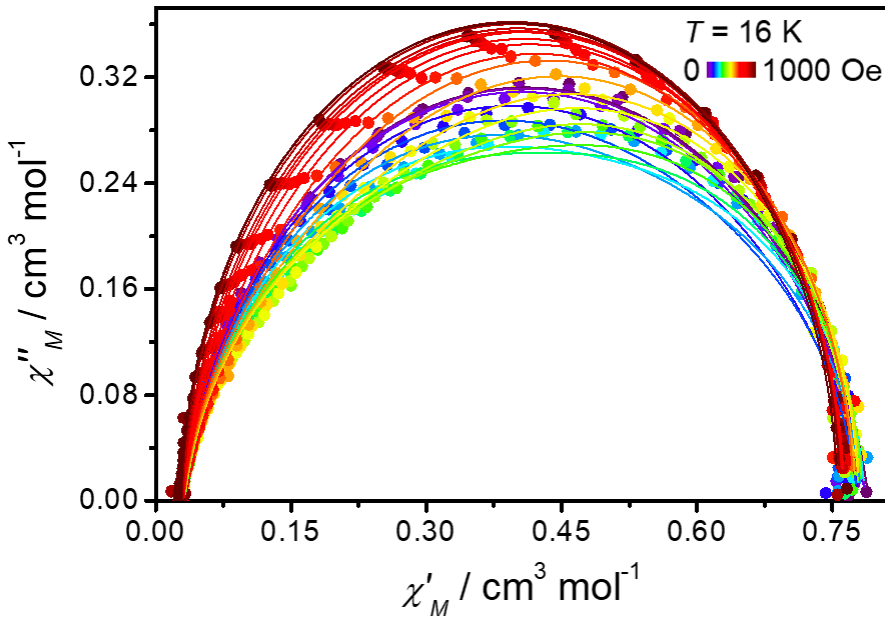


Figure S16. Cole-Cole plots of **1** at 16 K under 0-1000 Oe dc field, and the solid lines are best fits for the double-relaxation-time model.

Table S4. Selected 1D structures and their effective energy barrier.

Compound	U_{eff}/k_B [K]	References
$[\text{Mn}_2\text{Ni}_3\text{Cl}_2\text{L}_4(\text{LH})_2(\text{H}_2\text{O})_2]$	27	9
$\{\text{KDy}(\text{C}_2\text{O}_4)_2(\text{H}_2\text{O})_4\}_n$	418	10
$[\text{Dy}(\text{ppmc})_2 \cdot 4\text{H}_2\text{O}] \cdot \text{ppmc} \cdot \text{H}_2\text{O}$	74	11
$[\text{Dy}(\text{L})(\text{H}_2\text{O})_4]\text{Cl}_2 \cdot 2\text{H}_2\text{O}$	227	12
$\{[\text{Mn}^{\text{II}}(\text{dapsc})][\text{Mn}^{\text{III}}(\text{CN})_6][\text{K}(\text{H}_2\text{O})_{2.75} \cdot (\text{MeOH})_{0.5}]\}_n \cdot 0.5n(\text{H}_2\text{O})$	40	13
$[\text{Dy}(\mu\text{-H}_2\text{O})(\text{phen})(\mu\text{-OH})(\text{nb})_2]_n$	88.7	14
$[\text{Dy}(\text{L})_2(\text{phen})(\mu_2\text{-OH})(\mu_2\text{-H}_2\text{O})]_n$	567	15
$\{[\text{DyZn}_2(\text{L}^{\text{a}})_2(\text{POC})](\text{OH})(\text{ClO}_4)\} \cdot \text{H}_2\text{O} \cdot \text{MeOH}$	235	16
$[\text{TbCu}_2(\text{hfac})_7(\text{bisNITPhPy})]_n$	26	17
$[\text{Dy}_2(\mu_3\text{-cpdc}) (\mu_2\text{-bc}) (\text{H}_2\text{O})]_n$	55	18
$[\text{Yb}_2(\text{DAPBH})_2(\text{DPP})_3(\text{CH}_3\text{OH})](\text{NO}_3)(\text{ClO}_4)_2 \cdot 3\text{CH}_3\text{OH}$	7	19
$\{[\text{Dy}(\text{DAPMBH})(\text{N}_3)\text{C}_2\text{H}_5\text{OH}]\text{C}_2\text{H}_5\text{OH}\}_n$	47	20
$\text{Co}(\text{hfac})_2(\text{EtONapNIT})$	368	21
$[\text{Dy}(bbpen)(dppHO_2)][\text{BPh}_4] \cdot 2\text{MeCN} \cdot 2\text{H}_2\text{O}$	691	This work

4. Photoluminescence Spectra

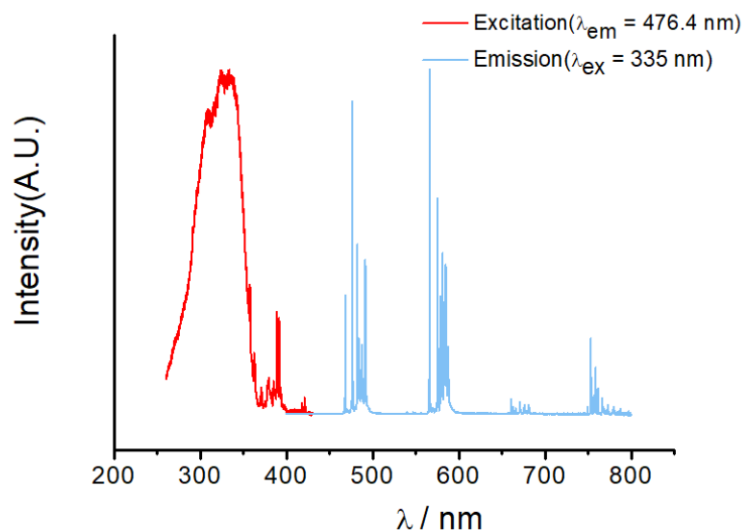


Figure S17. Photoluminescence spectra for **1** at 5 K.

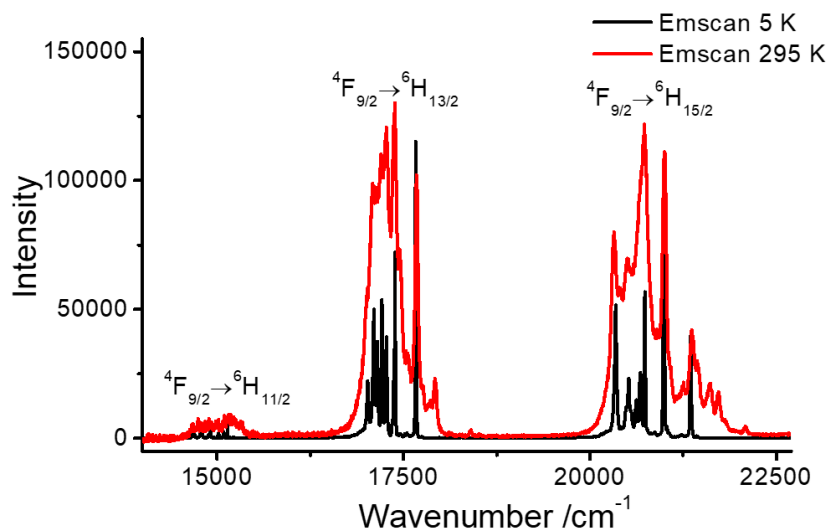


Figure S18. The emission spectra were measured at 295 K ($\lambda_{\text{ex}} = 350 \text{ nm}$) and 5 K ($\lambda_{\text{ex}} = 335 \text{ nm}$) for **1**.

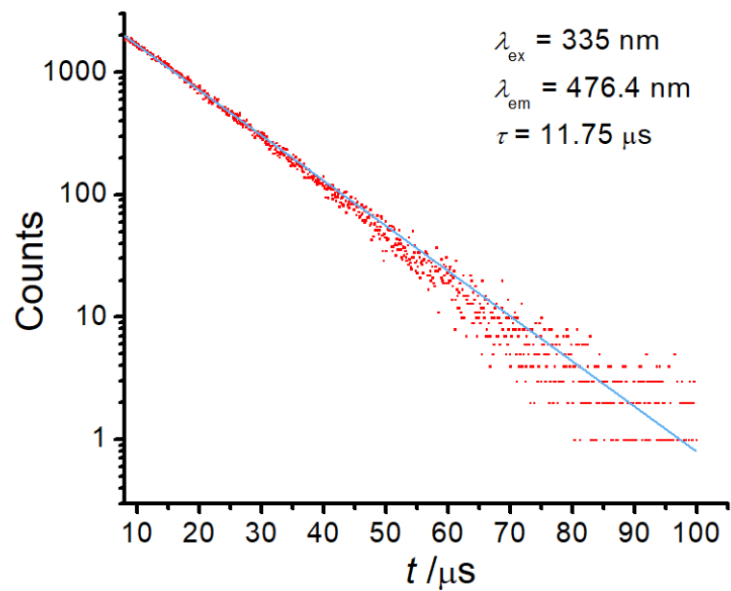


Figure S19. Lifetime measurements were collected at 5 K with mean lifetime $\tau = 11.75(3) \mu\text{s}$ (by first order exponential fits) for **1**.

5. Ab Initio Calculations

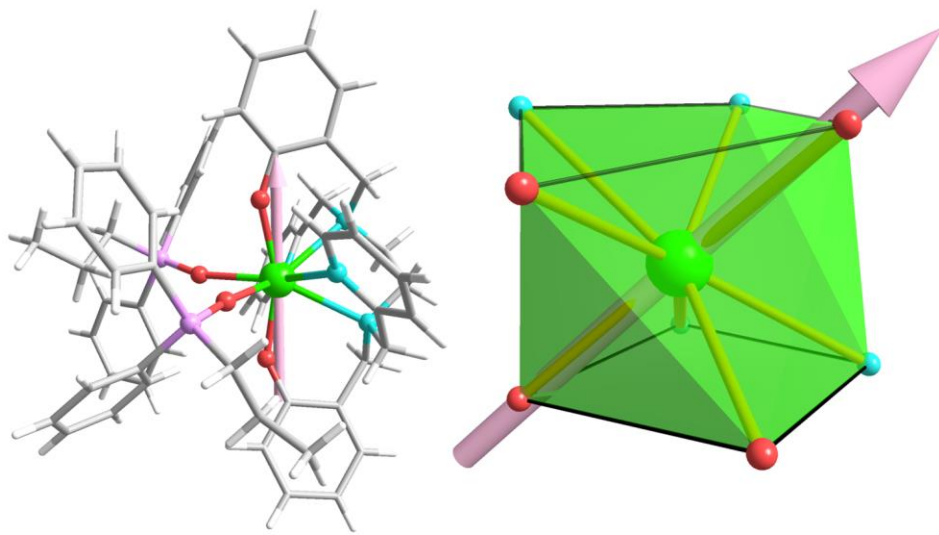


Figure S20. The fragment of single-crystal structure of **1** used for the *ab initio* calculations (*left*). The main magnetic axis of the ground Kramers doublet (pink arrow) is roughly along the pair of phenols' oxygen atoms and the central Dy displays distorted square antiprism geometry with the orientation of the main magnetic axis (*right*).

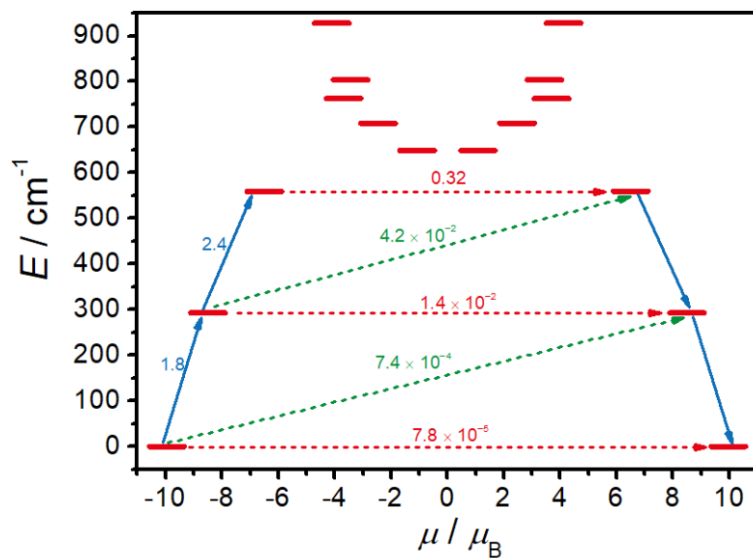


Figure S21. Magnetization blocking barriers for complex **1**. The lowest 16 spin-orbit states are arranged according to the magnitude of their magnetic moments on the horizontal axis. The numbers next to arrows connecting two states display the average transition magnetic moment matrix element between the respective states.

Table S5. Energies (cm^{-1}), g -tensors (g_x , g_y , g_z) and angles ($^\circ$) between the main magnetic axes of the selected Kramers doublet and the ground Kramers doublet for the local Dy(III) site in **1**.

KD	E	g	angle
1	0	0.0002	
		0.0003	0
		19.921	
2	292.477	0.0394	
		0.0424	2.363
		17.008	
3	559.088	0.6459	
		1.2224	5.769
		13.060	
4	648.725	1.1230	
		3.4630	83.502
		15.077	
5	708.554	2.1636	
		4.0088	69.696
		11.019	
6	762.568	1.2792	
		3.5893	45.052
		9.8967	
7	803.599	1.0015	
		3.3770	62.853
		14.791	
8	928.072	0.0956	
		0.2017	64.946
		19.400	

References

- 1 F. Aquilante, J. Autschbach, R. K. Carlson, L. F. Chibotaru, M. G. Delcey, L. De Vico, I. Fdez. Galván, N. Ferré, L. M. Frutos, L. Gagliardi, M. Garavelli, A. Giussani, C. E. Hoyer, G. Li Manni, H. Lischka, D. Ma, P. Å. Malmqvist, T. Müller, A. Nenov, M. Olivucci, T. B. Pedersen, D. Peng, F. Plasser, B. Pritchard, M. Reiher, I. Rivalta, I. Schapiro, J. Segarra-Martí, M. Stenrup, D. G. Truhlar, L. Ungur, A. Valentini, S. Vancoillie, V. Veryazov, V. P. Vysotskiy, O. Weingart, F. Zapata and R. Lindh, Molcas 8: New capabilities for multiconfigurational quantum chemical calculations across the periodic table. *J. Comput. Chem.*, 2016, **37**, 506-541.
- 2 B. O. Roos, R. Lindh, P.-Å. Malmqvist, V. Veryazov, P.-O. Widmark and A. C. Borin, New relativistic atomic natural orbital basis sets for lanthanide atoms with applications to the Ce diatom and LuF₃. *J. Phys. Chem. A.*, 2008, **112**, 11431-11435.
- 3 B. O. Roos, R. Lindh, P.-Å. Malmqvist, V. Veryazov and P.-O. Widmark, Main group atoms and dimers studied with a new relativistic ANO basis set. *J. Phys. Chem. A.*, 2004, **108**, 2851-2858.
- 4 B. O. Roos, R. Lindh, P.-Å. Malmqvist, V. Veryazov and P.-O. Widmark, New relativistic ANO basis sets for transition metal atoms. *J. Phys. Chem. A.*, 2005, **109**, 6575-6579.
- 5 P. Å. Malmqvist, B. O. Roos and B. Schimmelpfennig, The restricted active space (RAS) state interaction approach with spin-orbit coupling. *Chem. Phys. Lett.*, 2002, **357**, 230-240.
- 6 L. F. Chibotaru and L. Ungur, *Ab initio* calculation of anisotropic magnetic properties of complexes. I. Unique definition of pseudospin hamiltonians and their derivation. *J. Chem. Phys.*, 2012, **137**, 064112.
- 7 D. Casanova, M. Llunell, P. Alemany and S. Alvarez, The rich stereochemistry of eight-vertex polyhedra, A continuous shape measures study. *Chem. Eur. J.*, 2005, **11**, 1479-1494.
- 8 (a) D. Gatteschi, R. Sessoli and J. Villain, Molecular nanomagnets. London, Oxford Univ Pr; 2006, 72-73.
(b) Y.-N. Guo, G.-F. Xu, Y. Guo and J. Tang, Relaxation dynamics of dysprosium(III) single molecule magnets, *Dalton Trans.*, 2011, **40**, 9953-9963.
- 9 A. Das, K. Gieb, Y. Krupskaya, S. Demeshko, S. Dechert, R. Klingeler, V. Kataev, B. Büchner, P. Müller and F. Meyer, A new family of 1D exchange biased heterometal single-molecule magnets, Observation of pronounced quantum tunneling steps in the hysteresis loops of quasi-linear {Mn₂Ni₃} clusters. *J. Am. Chem. Soc.*, 2011, **133**, 3433-3443.
- 10 S. Mohapatra, B. Rajeswaran, A. Chakraborty, Bimodal magneto-luminescent dysprosium (Dy^{III})-potassium(K⁺)-oxalate framework, Magnetic switchability with high anisotropic barrier and solvent sensing. *Chem. Mater.*, 2013, **25**, 1673-1679.
- 11 L. Jia, Q. Chen, Y.-S. Meng, H.-L. Sun and S. Gao, Elucidation of slow magnetic relaxation in a ferromagnetic 1D Dysprosium chain through magnetic dilution. *Chem. Commun.*, 2014, **50**, 6052-6055.
- 12 Q. Chen, Y.-S. Meng, Y.-Q. Zhang, S.-D. Jiang, H.-L. Sun and S. Gao, A 1D Dysprosium chain with slow magnetic relaxation constructed from a pyridine-N-oxide ligand. *Chem. Commun.*, 2014, **50**, 10434-10437.
- 13 V. D. Sasnovskaya, V. A. Kopotkov, A. D. Talantsev, R. B. Morgunov, E. B. Yagubskii, S. V. Simonov, L. V. Zorina and V. S. Mironov, Synthesis, structure, and magnetic properties of 1D {[Mn^{III}(CN)₆][Mn^{II}(dapsc)]}_n coordination polymers, Origin of unconventional single-chain magnet behavior. *Inorg. Chem.*, 2017, **56**, 8926-8943.
- 14 Y. Li, P. Zhao, S. Zhang, R. Li, Y.-Q. Zhang, E.-C. Yang and X.-J. Zhao, A rare water and hydroxyl-extended one-dimensional Dysprosium(III) chain and its magnetic dilution effect. *Inorg. Chem.*, 2017, **56**, 9594-9601.
- 15 X. Zhang, S. Liu, V. Vieru, N. Xu, C. Gao, B.-W. Wang, W. Shi, L. F. Chibotaru, S. Gao, P. Cheng and A. K. Powell, Coupling influences SMM properties for pure 4 f systems. *Chem. Eur. J.*, 2018, **24**, 6079-6086.
- 16 C.-M. Liu, D.-Q. Zhang, J.-B. Su, Y.-Q. Zhang and D.-B. Zhu, Single-molecule magnet behavior of 1D coordination polymers based on DyZn₂(salen)₂ units and pyridin-N-oxide-4-carboxylate, Structural divergence and magnetic regulation. *Inorg. Chem.*, 2018, **57**, 11077-11086.
- 17 J. Sun, J. Xie, L. Li and J.-P. Sutter, Single-chain magnet behavior in a 2p-3d-4f spin array with a nitronyl nitroxide biradical. *Inorg. Chem. Front.*, 2020, **7**, 1949-1956.

- 18 J.-Y. Wang, Y. Shi, D.-L. Tao, G.-Y. Yin and Q.-B. Bo, 2D chain layer versus 1D chain, Rigid aromatic benzoate disassembling flexible alicyclic dicarboxylate-based lanthanide coordination polymers with enhanced photoluminescence and characteristic single-molecule magnet behavior. *CrystEngComm*, 2020, **22**, 4449-4467.
- 19 G. Peng, Y. Chen and B. Li, One-dimensional lanthanide coordination polymers supported by pentadentate schiff-base and diphenyl phosphate ligands, Single molecule magnet behavior and photoluminescence. *New. J. Chem.*, 2020, **44**, 7270-7276.
- 20 T. A. Bazhenova, V. S. Mironov, I. A. Yakushev, R. D. Svetogorov, O. V. Maximova, Y. V. Manakin, A. B. Kornev, A. N. Vasiliev and E. B. Yagubskii, End-to-end azido-bridged lanthanide chain complexes (Dy, Er, Gd, and Y) with a pentadentate schiff-base $[N_3O_2]$ ligand, Synthesis, structure, and magnetism. *Inorg. Chem.*, 2020, **59**, 563-578.
- 21 X. Liu, X. Feng, K. R. Meihaus, X. Meng, Y. Zhang, L. Li, J.-L. Liu, K. S. Pedersen, L. Keller, W. Shi, Y.-Q. Zhang, P. Cheng and J. R. Long, Coercive fields above 6 T in two Cobalt(II)-radical chain compounds. *Angew. Chem., Int. Ed.*, 2020, **59**, 10610-10618.